J Neurophysiol 119: 476–489, 2018.
First published October 25, 2017; doi:10.1152/jn.00472.2017.

RESEARCH ARTICLE | *Neural Circuits*

Experience-dependent trends in CA1 theta and slow gamma rhythms in freely behaving mice

Brian J. Gereke,[1,2] Alexandra J. Mably,[2,3] and Laura Lee Colgin[1,2,3]
[1]*Institute for Neuroscience, University of Texas at Austin, Austin, Texas;* [2]*Center for Learning and Memory, University of Texas at Austin, Austin, Texas; and* [3]*Department of Neuroscience, University of Texas at Austin, Austin, Texas*

Submitted 25 June 2017; accepted in final form 19 October 2017

Gereke BJ, Mably AJ, Colgin LL. Experience-dependent trends in CA1 theta and slow gamma rhythms in freely behaving mice. *J Neurophysiol* 119: 476–489, 2018. First published October 25, 2017; doi:10.1152/jn.00472.2017.—CA1 place cells become more anticipatory with experience, an effect thought to be caused by NMDA receptor-dependent plasticity in the CA3–CA1 network. Theta (~5–12 Hz), slow gamma (~25–50 Hz), and fast gamma (~50–100 Hz) rhythms are thought to route spatial information in the hippocampal formation and to coordinate place cell ensembles. Yet, it is unknown whether these rhythms exhibit experience-dependent changes concurrent with those observed in place cells. Slow gamma rhythms are thought to indicate inputs from CA3 to CA1, and such inputs are thought to be strengthened with experience. Thus, we hypothesized that slow gamma rhythms would become more evident with experience. We tested this hypothesis using mice freely traversing a familiar circular track for three 10-min sessions per day. We found that slow gamma amplitude was reduced in the early minutes of the first session of each day, even though both theta and fast gamma amplitudes were elevated during this same period. However, in the first minutes of the second and third sessions of each day, all three rhythms were elevated. Interestingly, theta was elevated to a greater degree in the first minutes of the first session than in the first minutes of later sessions. Additionally, all three rhythms were strongly influenced by running speed in dynamic ways, with the influence of running speed on theta and slow gamma changing over time within and across sessions. These results raise the possibility that experience-dependent changes in hippocampal rhythms relate to changes in place cell activity that emerge with experience.

NEW & NOTEWORTHY We show that CA1 theta, slow gamma, and fast gamma rhythms exhibit characteristic changes over time within sessions in familiar environments. These effects in familiar environments evolve across repeated sessions.

gamma rhythms; hippocampus; mice; place cells; running speed; theta rhythms

INTRODUCTION

Rodent hippocampal place cells fire at specific spatial locations known as "place fields" as an animal moves through an environment (O'Keefe and Dostrovsky 1971). Place fields are plastic, expanding in the direction opposite of an animal's motion across repeated passes through the field and thus becoming more anticipatory with experience (Mehta et al. 1997, 2000). The emergence of anticipatory firing differs across the hippocampal subregions. In CA3, it emerges the first time an animal experiences a novel environment and then persists across days (Lee et al. 2004; Roth et al. 2012). In CA1, anticipatory firing is reacquired each day an animal is exposed to a familiar environment (Lee et al. 2004; Roth et al. 2012) but persists across multiple exposures within a day (Yu et al. 2006). As CA1 lacks recurrent excitation, anticipatory firing in CA1 is thought to depend on NMDA receptor-mediated Hebbian synaptic plasticity in feedforward projections from CA3 to CA1 (Mehta 2015; Mehta et al. 2000). In support of this view, manipulations that suppress NMDA receptor-dependent synaptic plasticity in CA1 have been shown to prevent anticipatory firing (Cabral et al. 2014; Ekstrom et al. 2001).

Both in vitro (Larson et al. 1986; Staubli and Lynch 1987) and in vivo (Hölscher et al. 1997; Hyman et al. 2003) evidence has suggested that theta rhythms (~5–12 Hz) promote synaptic plasticity in Schaffer collateral synapses between CA3 and CA1 neurons. Considering that such plasticity is thought to underlie anticipatory firing in CA1 place cells, as described above, theta may also promote the acquisition of anticipatory firing in CA1 place cells. If so, then one would expect theta rhythms to be maximal during the period when anticipatory firing develops, namely the first few minutes of exposure to an environment.

Additionally, CA1 slow gamma rhythms (~25–50 Hz), as opposed to fast gamma rhythms (~50–100 Hz), are thought to reflect times when CA1 responds preferentially to input from CA3. Specifically, slow gamma is coherent between CA1 and CA3 (Colgin et al. 2009; Kemere et al. 2013) and coincides with current sources/sinks in stratum radiatum where CA3 projections terminate (Belluscio et al. 2012; Schomburg et al. 2014). Therefore, it is possible that slow gamma in CA1 emerges with experience, in parallel with experience-dependent anticipatory firing in place cells, as synaptic connections between CA3 and CA1 are modified. Consistent with this possibility, CA1 slow gamma power has been shown to increase during times of anticipatory place cell firing in rats (Bieri et al. 2014).

In the present study, we assessed experience-dependent changes in theta, slow gamma, and fast gamma rhythms in CA1 in freely moving mice. We found that CA1 theta rhythms

Address for reprint requests and other correspondence: B. J. Gereke, Department of Neuroscience and Center for Learning and Memory, University of Texas at Austin, 1 University Station Stop C7000, Austin, TX 78712 (e-mail: bgereke@utexas.edu).

were strongest during the initial period of exposure to a familiar environment, whereas CA1 slow gamma rhythms developed with experience, as did anticipatory place cell firing in CA1. In contrast, fast gamma rhythms were not strongly affected by experience across sessions.

MATERIALS AND METHODS

Subjects and testing procedures. Data were obtained from 3 C57BL/6 and 3 C57BL/6 × 129 hybrid 8- to 9-mo-old mice during the dark phase of a reverse light-dark cycle (lights off 9 AM to 9 PM). We conducted this study using mice because a more complete understanding of how anticipatory firing in CA1 relates to slow gamma, and inputs from CA3, will require anatomically and temporally precise manipulations of slow gamma-generating circuits, and such manipulations are more amenable in mice. Recordings from the C57BL/6 × 129 hybrid mice were included in a previous study (Mably et al. 2017). Mice were housed in groups initially and then housed individually following surgery. After surgery, mice recovered for at least one week before the start of behavioral training and data acquisition. During training, mice were food deprived to ~90% of their free-feeding weight and trained to run unidirectionally around a circular track (100-cm diameter, 9-cm width) for three 10-min sessions per day interleaved with 10-min rest sessions. During the rest sessions, mice sat in an elevated flowerpot placed near the track. Small amounts of cookie cream were delivered as food rewards at a single location on the track. The reward location was fixed within each day but changed pseudo-randomly between days to prevent accumulation of place fields at particular reward sites (Dupret et al. 2010; Hollup et al. 2001; Zaremba et al. 2017). To ensure familiarity of the track and recording room, all mice were trained for at least 3 consecutive days before the first day of data collection. A total of 35 days of data, consisting of 5–7 days/mouse, were collected. All experiments were conducted according to the guidelines of the NIH Guide for the Care and Use of Laboratory Animals under a protocol approved by the University of Texas Austin Institutional Animal Care and Use Committee (protocol no. AUP-2015-00107).

Microdrive preparation, surgery, and tetrode placement. Microdrives were custom built using a modified version of a previously published design (Voigts et al. 2013). Drives contained two bundles spaced 4 mm apart. Each bundle contained eight independently moveable tetrodes. Tetrodes were constructed from 17-μm polyimide-coated platinum-iridium wire (California Fine Wire). Electrode tips were plated with platinum to reduce single channel impedances to ~150–300 kΩ at 1 kHz.

Microdrives were surgically implanted bilaterally in CA1 with coordinates: 2.0 mm anteroposterior, ± 2.0 mm mediolateral, and 0.5 mm dorsoventral. To anchor microdrives to the skull, 6–7 jewelers screws were placed in the skull, with the two most anterior used as electrical grounds. The microdrives were then secured to the skull with dental acrylic. Tetrodes were lowered ~40–100 μm/day, reaching their target location in or near the CA1 cell body layer at ~2 wk after drive implantation. Tetrodes were not moved more than 40 μm/day on days preceding data acquisition. One tetrode in each bundle was used as a differential recording reference and was placed in a relatively quiet, spike-free area of the overlying cortex. This was confirmed by recording reference tetrodes continuously against ground. CA1 stratum pyramidale was identified by its electrophysiological signatures (e.g., robust theta rhythms, sharp wave ripple polarity, etc.), as well as the presence of place cell spikes.

Histology. All recording locations were histologically verified after experiments were completed. First, mice were placed under isoflurane gas anesthesia and given a lethal dose of sodium pentobarbital (intraperitoneal injection). This was followed by transcardial perfusion, first with physiological saline to remove blood from the brain and then with 4% formaldehyde solution to fix the brain. The brain was left to fix for ~1 h following perfusion to allow shrinkage of brain tissue away from tetrodes, thereby ensuring that tetrode tracks would be visible in histological sections (e.g., tracks of two separate tetrodes within the same bundle can be seen in Fig. 1*A*). For verification of tetrode locations, brains were cut coronally (3 mice) or sagittally (3 mice) at 30 μm and stained with cresyl violet. Each section through the relevant part of the hippocampus was collected. All tetrode locations were identified, and the tip of each tetrode was localized by comparison across adjacent sections.

Data acquisition. The data acquisition setup consisted of a Digital Lynx 4SX acquisition system, a 64-channel PSR slip-ring commutator, and two HS-36 analog headstages with lightweight fine wire tethers (Neuralynx, Bozeman, MT). For spike detection, signals were digitally bandpass filtered between 600 and 6,000 Hz, and filtered signals that exceeded a threshold (30–60 μV) set by the experimenter were sampled at 32 kHz. Spike sorting was then performed offline using an open source cluster cutting package in MATLAB (MClust; A.D. Redish, University of Minnesota, Minneapolis). Clustering was performed manually on two-dimensional projections of the spike waveform features (i.e., Energy, Peak, and PeakValleyDiff). Autocorrelation functions were also used to identify well-isolated single units (i.e., units included in the study were required to exhibit a refractory period containing no spikes). For field potential recordings, signals were digitally bandpass filtered between 0.1 and 500 Hz and sampled at 2 kHz. For position and running speed estimation, position was tracked at a video frame rate of 30 Hz via colored LEDs on the headstages. Position samples were then smoothed using a 2nd order loess filter from the R package *stats* with a span of 6 s. Running speed was then estimated as the time derivative of the smoothed position samples. Where noted, running speed was normalized within each day to between 0 and 1 (as in Chen et al. 2011).

Place cell analyses. One-dimensional circular place maps were computed by binning the spikes into 1 cm bins and dividing the number of spikes in each bin by the amount of time spent in each bin. Place fields were detected by finding the maximal firing rate location across the three sessions. Place field boundaries were set at locations where the firing dropped below 10% of the peak firing rate for 10 consecutive cm on either side of the maximal firing location. Center-of-mass (COM) estimates for single laps were computed from single lap place maps, discarding spikes occurring outside the place field boundaries. Field peak was defined as the location of maximal firing rate on each pass. First spike and last spike were defined as the locations of the first and last spikes occurring within the field boundaries on each pass, respectively. Field size was defined as the integral of the firing rate map with respect to space within the field boundaries for each pass; it was then normalized by dividing by the mean field size across all passes independently for each cell. The within field firing rate was defined as the number of spikes divided by the time spent inside the place field boundaries for each pass; it was then normalized by dividing by the mean within field firing rate across all passes independently for each cell. Field width was defined as the distance between the first and last spike occurring within the field boundaries on each pass. Field width was normalized by dividing by the mean field width across all passes independently for each cell. Skewness was defined as the ratio of the third moment divided by the cube of the standard deviation of the firing rate map within the field boundaries on each pass. The firing rate asymmetry index (FRAI) was defined as in Mehta et al. 2000. Briefly, F1 was the firing rate during the first 50% of spikes, and F2 was the firing rate during the second 50% of spikes occurring on each pass, with FRAI = (F1 – F2)/(F1 + F2). For place cells with multiple fields (138/377), only the field with the highest peak rate was considered. Fields within 15 cm of the reward location were excluded to avoid contamination by spikes occurring during sharp wave-ripples, considering that sharp wave-ripples occur during reward consumption (i.e., eating; Buzsáki 1986) and place cells often fire outside of their fields during sharp wave-ripples (Foster and Wilson 2006). As in Lee et al. 2004, cells that fired <50 spikes/session within their field boundaries, were also excluded.

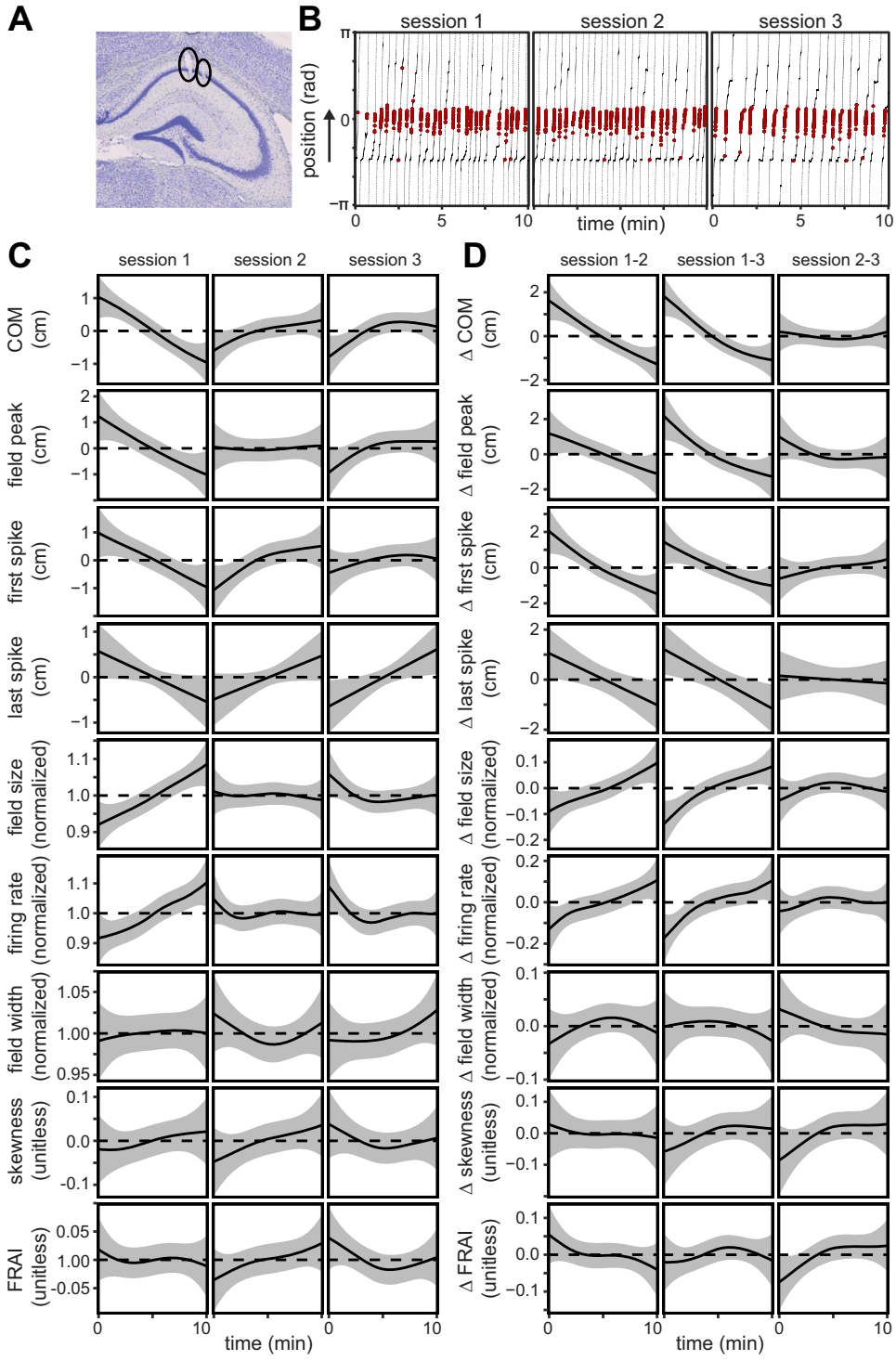

Fig. 1. CA1 place field properties vary with experience. *A*: histological section showing example tetrode sites in CA1 cell body layer. Tracks of two individual tetrodes can be seen and are circled in black. *B*: example spike raster for a single place cell showing the locations of spikes (red dots) across multiple laps around a circular track in *sessions 1–3*. Fewer spikes were emitted on the first two laps of *session 1* after which the firing rate increased while the place field expanded backward. No such effect is evident in *sessions 2*–3. The arrow next to the *y*-axis denotes the direction of movement. *C*: experiential changes in place field properties [top-to-bottom: center of mass (COM), field peak, first spike, last spike, normalized field size, normalized firing rate, normalized field width, skewness, firing rate asymmetry index (FRAI)] across time for *sessions 1–3* (left to right) for all included place cells. *D*: differences between the curves shown in *C*. *Left column* shows the *session 2* curves subtracted from the *session 1* curves, while the *middle* and *right columns* show the *session 3* curves subtracted from the *session 1* and *2* curves, respectively. Gray shaded areas denote 95% simultaneous confidence bands. Corresponding pointwise level $\alpha < 0.01$ for all bands.

Passes with a mean running speed of <5 cm/s in either half of the field or less than three spikes were also discarded. A total of 286/377 place fields and 8,758/14,847 passes met these inclusion criteria.

Changes in place field properties over time across the three sessions were quantified by an additive model (see *Statistical analyses* below):

$$y_i \sim session_i + s_{session}(time_i) + \varepsilon_i, \varepsilon \in N(0, \sigma)$$

The response y could be any of the place field properties listed in Tables 1–2 and described above. Separate smooth functions $s_{session}(\cdot)$ were estimated for each session.

Signal processing. All signal processing was performed using custom MATLAB scripts. Time-resolved power was estimated using a complex Morlet wavelet transform with a width parameter of seven periods, evaluated at 50 frequencies logarithmically spaced between 2 and 100 Hz, and applied to a single channel from a tetrode in the cell body layer of CA1. A tetrode was classified as being in the cell layer if it had a place cell and was later histologically verified to be in or close to the CA1 cell body layer. Among these tetrodes, the channel with the largest theta amplitude was selected to be included in the analysis. Theta phase was then

Table 1. *Statistical summary of time-by-session curves from Fig. 1C*

	$s_{session1}(time)$			$s_{session2}(time)$			$s_{session3}(time)$		
Response Variable	Ref. df	*F*	*P*	Ref. df	*F*	*P*	Ref. df	*F*	*P*
COM	2.49	19.18	$<10^{-9}$	2.54	3.84	0.02	2.54	6.25	$<10^{-3}$
Field peak	2.10	10.13	$<10^{-4}$	2.15	0.14	0.91	2.14	3.99	0.02
First spike	2.14	8.49	$<10^{-3}$	2.19	6.63	<0.01	2.18	1.15	0.29
Last spike	1.02	5.50	0.02	1.02	4.53	0.03	1.02	7.71	<0.01
Field size	2.69	12.68	$<10^{-6}$	2.75	0.18	0.87	2.75	3.25	0.07
Firing rate	3.87	9.76	$<10^{-6}$	3.95	1.38	0.30	3.96	4.32	<0.01
Field width	2.25	0.13	0.89	2.29	1.73	0.15	2.29	1.50	0.20
Skewness	2.10	0.74	0.48	2.15	2.06	0.13	2.15	1.39	0.28
FRAI	2.63	0.61	0.62	2.68	2.31	0.09	2.68	2.31	0.08

Ref. df is the reference degrees of freedom used for approximate *F*-ratio and *P* value computation and is also a measure of curve nonlinearity. Ref. df closer to 1 is more linear. COM, center of mass; FRAI, firing rate asymmetry index. See Wood 2013 and Wood 2017 (sec. 6.12) for further details. n = 2,701, 2,990, and 3,067 laps for *sessions 1–3*, respectively.

estimated using the Hilbert transform of the theta (6–12 Hz) bandpass-filtered signal.

To reduce computational burden for statistical analyses, power estimates were downsampled to the video frame rate of 30 Hz, and all samples within 15 cm of the reward location were discarded. Power was normalized separately for each frequency and day. Normalization was performed by taking a kernel density estimate of the cumulative distribution function (cdf) of the log power using the kcde function from the ks package in R (Duong 2007, 2016). The cdfs were then mapped to *z*-scores so that the power distribution for each frequency became normally distributed with mean zero and unit variance, as verified by Q-Q plots.

Statistical analyses. All statistical analyses were performed using an additive mixed model (AMM) framework. AMMs do not assume a particular form for the estimated effects (i.e., linear, monotonic, etc.) and can help control for variance unique to a specific experiment. They have the general form

$$y_i \sim \boldsymbol{A}_i\boldsymbol{\alpha} + \sum_j \omega_{ij} s_j(x_{ij}) + \boldsymbol{Z}_i\boldsymbol{b} + \varepsilon_i, \varepsilon \in N(0, \sigma^2\Lambda)$$

Here, y_i is the ith observation. $\mathbf{A}$ is a design matrix for parametric terms with associated parameter vector $\boldsymbol{\alpha}$. The $s_j(\cdot)$ are "smooth" functions over the covariates x_j (i.e., running speed, theta phase, or time within a session) with dummy variables ω_{ij} that allow the functions to vary with respect to another variable (e.g., session). $\mathbf{Z}$ is a design matrix for random effects terms with associated parameter vector $\mathbf{b}$. ε is the usual error term and is assumed to be normally distributed with variance σ^2 and correlation matrix $\boldsymbol{\Lambda}$, allowing for correlations between the errors to be modeled.

AMMs of this form were fit using the bam function for large data from the mgcv package (Wood 2004, 2017; Wood et al. 2015; version 1.8) in R (R Core Team 2016). In mgcv, the $s_j(\cdot)$ are represented by penalized spline bases (Wood et al. 2015). For efficiency purposes, we used natural cubic splines for all covariates, except theta phase, for which cyclic natural cubic splines were used. Functional interactions were fit using tensor product interaction bases with corresponding natural cubic and/or cyclic natural cubic marginal bases.

Each covariate had an associated smoothness parameter λ_j, which controls the degrees of freedom (df) allocated to the term. A large value of λ_j results in a linear estimate for the term, while a small λ_j allocates some maximum df that was chosen a priori. This maximum was set to 10 df for all univariate terms and 5 df for each dimension of the interaction terms. To ensure an interpretable surface, the maximal df for the running speed-by-time interaction was set to 3 df for both dimensions as the higher running speeds were more sparsely sampled. The values of the λ_j were selected during model fitting with regard to some criterion, allowing the data to determine how strongly each term is penalized. For this criterion, we used restricted maximum likelihood estimation (REML) as it has good numerical convergence properties and offers robustness against misspecification of the error correlation structure (Krivobokova and Kauermann 2007; Wood 2011).

For the random effects terms, the mgcv package implements random factor smooths (Baayen et al. 2016). These terms help control for repeated measurements and are used to estimate deviations from the population mean function at different levels of a grouping factor. This is accomplished by incorporating additional lower order penalties on the linear parts of the functions so that they shrink to constants. Thus small penalties estimate smooth random functions while large penalties result in random intercepts for each level of the grouping factor. Mice were run on a single experiment per day; therefore, we included random factor smooths for each univariate predictor with *day* as the grouping factor. This was done to ensure that the variation related to each covariate that was unique to a particular day was taken into account.

Table 2. *Statistical summary of time-by-session difference curves from Fig. 1D*

	$s_{session1-2}(time)$			$s_{session1-3}(time)$			$s_{session2-3}(time)$		
Response Variable	Ref. df	*F*	*P*	Ref. df	*F*	*P*	Ref. df	*F*	*P*
COM	2.15	23.12	$<10^{-10}$	2.14	24.56	$<10^{-11}$	2.18	0.02	0.97
Field peak	1.70	6.70	<0.01	1.01	23.47	$<10^{-5}$	1.01	2.02	0.15
First spike	1.62	17.96	$<10^{-6}$	1.71	8.84	$<10^{-3}$	1.74	1.21	0.21
Last spike	1.01	10.11	<0.01	1.01	13.23	$<10^{-3}$	1.01	0.22	0.64
Field size	2.66	7.85	$<10^{-4}$	2.86	9.83	$<10^{-5}$	2.91	0.84	0.44
Firing rate	3.25	7.59	$<10^{-4}$	3.48	10.69	$<10^{-6}$	3.54	0.79	0.54
Field width	1.73	0.34	0.57	1.88	0.76	0.54	1.91	1.41	0.18
Skewness	1.45	0.19	0.78	1.01	1.85	0.17	1.01	3.68	0.05
FRAI	1.85	2.14	0.13	1.29	0.32	0.62	1.31	5.25	0.01

n = 2,701, 2,990, and 3,067 laps for *sessions 1–3*, respectively.

To control for correlations between temporally adjacent samples, mgcv allows a first order autoregressive (AR1) correlation structure to be assumed for the errors (Baayen et al. 2016). This term has a parameter, ρ, which describes the expected correlation between adjacent errors. For efficiency purposes, this parameter was estimated by the Yule-Walker method on the residuals of the corresponding model fit without the AR1 term, using the "ar" function from the base stats package in R. Including the AR1 correlation produced similar mean estimates, but more conservative covariance estimates, of the model coefficients.

Confidence intervals and test statistics. Due to the large size of the local field potential data, AMMs were fit independently for each frequency. To control for multiple comparisons, approximate 95% simultaneous confidence intervals were estimated over all model terms and frequencies jointly using a simulation-based approach (Ruppert et al. 2003). Briefly, the model coefficient estimates were distributed multivariate normal with mean vector $\hat{\beta}$ and covariance matrix $\mathbf{\Omega}$. Simulations may be made by multiplying a sample from this distribution with the linear predictor matrix defined on a dense grid of the predictor values. We simulated all the model terms simultaneously 1,500 times for each frequency. The absolute values of the pointwise deviations of the simulations were then standardized, and the maximum standardized deviation across all terms for each simulation was identified. A critical value $m_{1-\alpha}$ was defined as the 95% quantile of the maximum deviations. For the "full" model, $m_{1-\alpha}$ was ~4.8, which resulted in intervals ~2.5 times wider than the critical value of 1.96 used for pointwise intervals and a corresponding pointwise level $\alpha \approx 1.59 \cdot 10^{-6}$. Similar intervals were produced for the place field properties analyses for which models were sampled 10,000 times, which was computationally manageable due to the smaller size of the models.

All test statistics reported in Tables 1 and 2 (e.g., *F*-ratios, *P* values, etc.) are the default values reported by mgcv and test against the null hypothesis that all coefficients making up a smooth term are identically equal to 0. These values should be regarded as approximations as they are conditional upon the smoothing parameters (i.e., λ_j) selected by the REML estimation. See Wood 2013 and Wood 2017 (sec. 6.12) for further details.

Cross-validation analyses. To compare the predictive strength of *running speed*, *time-within-session* (also referred to as *time*), *theta phase*, and *session* with regard to our observed oscillatory power measurements, we performed leave-one-mouse-out cross-validation analyses on a series of six models:

base:

$$power_f \sim session + s(speed) + s(phase) + ti(speed,\ phase) + fs(speed|day) + fs(phase|day) + \varepsilon,\ \varepsilon \in N(0,\ AR1)$$

+ time:

$$power_f \sim RHS_{base} + s(time) + fs(time|day)$$

+ time-by-session:

$$power_f \sim RHS_{base} + s_{session}(time) + fs(time|day)$$

+ speed-by-time-by-session:

$$power_f \sim RHS_{base} + s_{session}(time) + ti_{session}(speed, time) + fs(time|day).$$

+ phase-by-time-by-session:

$$power_f \sim RHS_{base} + s_{session}(time) + ti_{session}(phase, time) + fs(time|day)$$

full:

$$power_f \sim RHS_{base} + s_{session}(time) + ti_{session}(phase, time) + ti_{session}(speed, time) + fs(time|day)$$

In all equations, observation indices are implicit, *f* indexes frequency, RHS_{base} is the right-hand side of the base model, the $s_{session}(\cdot)$ denote separate smooth functions for each session, the $ti_{session}(\cdot)$ are separate tensor product interactions for each session, and the $fs(\cdot|day)$ are random factor smooth functions with day as the grouping factor. Each model was fit using the data from all but one mouse. The data from the withheld mouse were then used to test predictions from the fitted model. Estimates corresponding to the random factor smooth functions were excluded from the predictions. This procedure was repeated for all six mice, and the combined prediction errors were used to calculate R^2 values for each frequency. The cross-validation folds were fit in parallel using the High Performance Computing resources at the Texas Advanced Computing Center (TACC) at the University of Texas at Austin.

RESULTS

CA1 place cells become more anticipatory with experience in familiar environments, as evidenced by a backward shift of their place fields over time in both rats (Lee et al. 2004; Mehta et al. 1997, 2000), and mice (Cabral et al. 2014). We attempted to replicate this effect by performing multisite tetrode recordings (Fig. 1*A*) in mice ($n = 6$) running unidirectionally around a familiar circular track for three 10-min sessions per day. Figure 1*B* shows an example recording from a place cell in this task. The cell fired fewer spikes during the first two laps of the first session, after which its place field expanded backward, remaining stable throughout the following two sessions. To characterize how place fields change on average over time, we considered a number of single-pass place field properties that have previously been demonstrated to change in experience-dependent ways (Cabral et al. 2014; Lee et al. 2004; Mehta et al. 1997, 2000). Figure 1*C* visualizes each of these effects while Table 1 provides an associated summary of test statistics. Place field COM, as well as the locations of peak firing and of the first and last spikes within the field, all shifted backward by ~1–2 cm during the first session (Fig. 1*C*; Table 1; top 4 rows). This contrasts with *sessions 2* and *3* where these measures had either negligible or smaller shifts in the forward direction. Place fields also became more robust during the first session as evidenced by an increase in field size and within-field firing rate (Fig. 1*C*; Table 1; rows 5–6). Again, trends in these measures were either negligible or in the opposite direction during the subsequent sessions. Field size was measured as the integral of the spatial firing rate map within the field boundaries on each pass. Thus it is influenced by changes in within-field firing rate and place field width. No significant trends were discernable for place field width during any of the sessions (Fig. 1*C*; Table 1; row 7), so changes in place field size likely reflected firing rate changes. We found no significant trends in measures of place field asymmetry (skewness and firing rate asymmetry index; Fig. 1*C*; Table 1; bottom 2 rows). Our results are therefore in line with prior suggestions that location-based measures (e.g., COM) may be more reliable indicators of place field plasticity (Cabral et al. 2014; Lee et al. 2004).

Figure 1*D* displays between-session comparisons in the form of difference curves for the place field measures described above and shown in Fig. 1*C*. These difference curves demonstrate that for all measures containing strong trends in the first session, significant differences are evident between the first and subsequent sessions but not between *sessions 2* and *3* (Fig. 1*D*; Table 2). Thus the experience-dependent, backward shift-

ing of place fields that has previously been reported was replicated in the present data set.

Theta and gamma power and phase-amplitude correlations increased with running speed. We next wanted to test for the presence of similar experience-dependent trends in CA1 theta and gamma rhythms. In mice, the amplitudes of slow and fast gamma, as well as theta-gamma phase-amplitude correlations, have been reported to increase with increasing running speed (Chen et al. 2011). Moreover, the influence of running speed on theta and gamma in rats has been shown to decrease across repeated exposures to an initially novel environment (Kemere et al. 2013). Thus we reasoned that the relationships between running speed, theta, and gamma would change over time both within and between sessions in an experience-dependent fashion.

In a setting such as this, with many potential effects (e.g., *running speed*, *time-within-session*, etc.), accounting for the simultaneous influence of the many variables involved can be difficult to accomplish using univariate methods. Multiple regression methods allow for the estimation of the additional contribution each variable makes after being adjusted for the presence of the other variables (e.g., effect of *time-within-session* adjusted for *running speed*). We therefore chose to study the joint effects of *running speed*, *time-within-session*, *theta phase*, and *session number* using an additive mixed model framework (see *Statistical analyses* section in MATERIALS AND METHODS). This allowed us to estimate the additive contributions of each variable while controlling for the others, as well as for variation in the estimates that may be unique to each experiment (e.g., a particular day of recording). To identify the extent to which the effects of each of these predictors changed continuously with frequency in an unbiased way, separate models were fit for 50 frequencies logarithmically spaced between 2 and 100 Hz. The statistical assumptions of the model were better met by including a first order autoregressive process (AR1) for the residuals to control for the presence of autocorrelation, which was stronger for the lower frequency rhythms (Fig. 2). Including this term did not strongly alter any of the estimated effects we report ($\rho_{AR1-,\ AR1+} > 0.99$ for all predictors) but reduced the total amount of autocorrelation, resulting in more conservative confidence estimates.

Figure 3*A* (*top*) shows a one second example local field potential (LFP) recording and associated running speed estimates to illustrate the relationship between running speed and gamma reported by Chen et al. (2011). The amplitudes of theta and slow gamma oscillations can be seen to increase as the animal runs faster. Figure 3*A* (*bottom*) shows a similar example in which the amplitude of fast gamma increases with running speed. To quantify these effects on grouped data, we began by fitting a *base* model which included *running speed*, *theta phase*, and a *running speed-by-theta phase* functional interaction as predictors for oscillation amplitude (i.e., power). Figure 3, *B–D* displays the resulting additive contributions of each of these terms to the overall fit of the model (i.e., the overall prediction of oscillation amplitude made by adding the separate contributions together).

Figure 3*B* shows that power in the delta to low theta range (2–8 Hz) decreased with running speed, while power in the upper theta range (~9–10 Hz) increased with running speed. These lower and higher frequency theta rhythms may correspond to the atropine-sensitive/resistant theta rhythms that occur during immobility/active movements, respectively (Kramis et al. 1975). We will refer to these as "slow" and "fast" theta for the remainder of the paper. Additionally, theta in rats is known to become less sinusoidal with increasing running speed (Sheremet et al. 2016). That is, the theta cycle often has a faster rise and/or sharper troughs than a pure sinusoid (Fig. 3, *A* and *C*). Accordingly, separate putative harmonics, one slow (~11–16 Hz) and one fast (~17–20 Hz), can be seen to decrease and increase, respectively, with running speed (Fig. 3*B*).

Consistent with the findings of Chen et al. (2011), power in the slow gamma (~25–50 Hz) and fast gamma (~50–100 Hz) ranges both increased with running speed (Fig. 3*B*). This effect differs from what is typically found in rats (Ahmed and Mehta 2012; Zheng et al. 2015), and others have suggested that this increase in slow gamma amplitude with running speed observed in mice may be attributable to a theta harmonic (Kemere et al. 2013). However, example LFP recordings show discernible slow gamma oscillations that increase with increasing running speed (Fig. 3*A*), suggesting that this may not be a full explanation.

Figure 3*C* shows the additive contribution of *theta phase* to power at each frequency. As in Chen et al. (2011), slow and fast gamma power were higher around the peak of theta (~0 radians), with slow gamma centered more on the descending phase (Fig. 3*C*). We will refer to the theta phases associated with maximal slow and fast gamma power as the "preferred" theta phases of slow and fast gamma. Figure 3*D* shows the additive contribution of the *running speed-by-theta phase* interaction and conveys how the relationship between theta phase and gamma power changed across different running speeds. Slow and fast gamma power both increased at their preferred theta phases (i.e., ~0-π rad for slow gamma, ~0 rad for fast gamma) with faster running speeds (Fig. 3*D*), demonstrating that theta-gamma phase-amplitude correlations become stronger at higher running speeds as reported in Chen et al. (2011). Chen et al. (2011) also reported a theta phase shift of slow gamma, but not fast gamma, power with respect to running

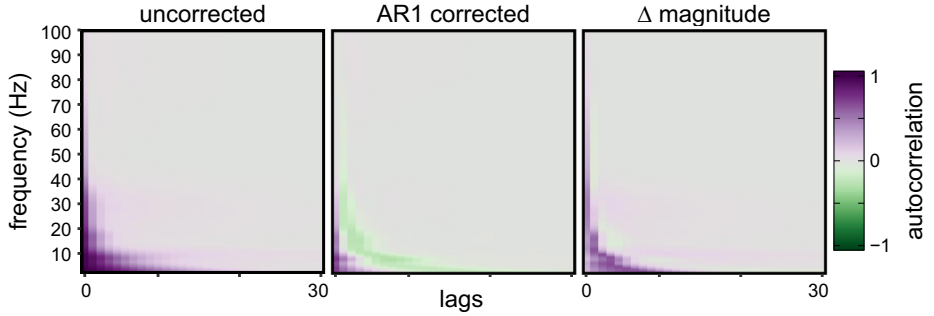

Fig. 2. AR1 correction of residuals in *base* model. *Left*: autocorrelation functions of the residuals for each frequency fit under the *base* model (see text). *Middle*: corrected residuals for the same model assuming an AR1 error process. *Right*: difference in the magnitude of autocorrelation between the two models, where purple corresponds to less autocorrelation in the AR1 corrected model. One lag is ~33 ms, such that the *x*-axes range from ~0–990 ms.

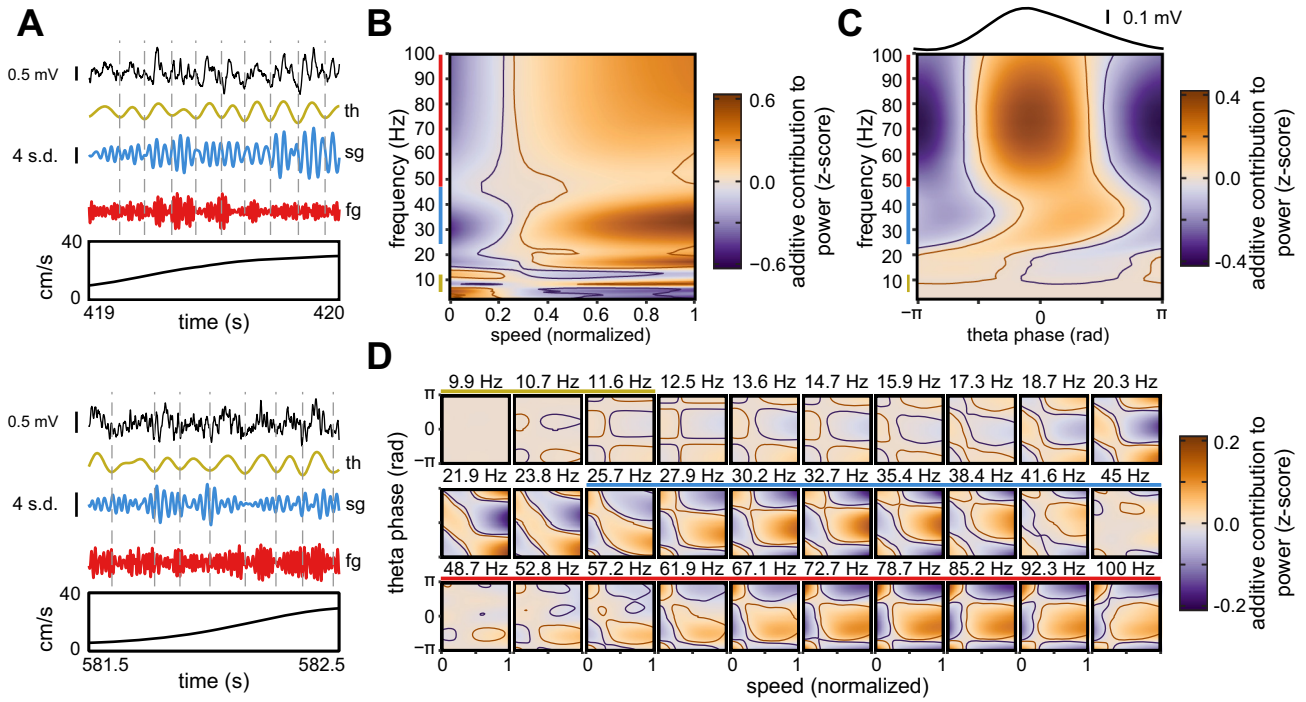

Fig. 3. Dependence between running speed, theta/gamma amplitude, and theta phase-gamma amplitude correlations. *A*: example local field potential (LFP) recordings, with bandpass-filtered versions for theta (th), slow gamma (sg), and fast gamma (fg) frequencies during periods of increasing running speed. In both the raw and filtered traces of the *top*, slow gamma amplitude increases with running speed. The *bottom* shows a similar example in which fast gamma amplitude increases with running speed. Vertical dashed lines denote theta troughs. *B–D*: each panel corresponds to a single term in the *base* model (see text). Yellow, blue, and red lines on frequency axes denote approximate theta, slow gamma, and fast gamma bands, respectively. *B*: additive contribution of running speed to power at each frequency. *C*: additive contribution of theta phase to power at each frequency. Black curve above is the mean broadband (i.e., 0.1–500 Hz) LFP at each phase of theta with scale bar for reference. Notice the asymmetry of the theta waveform. *D*: additive contribution of the *running speed-by-theta phase* interaction to power at each frequency. Each subpanel is the additive effect for a separate frequency, denoted by the labels above the subpanels. Frequencies <9.9 Hz are omitted to conserve space as no significant effects were observed at these frequencies. Only every other subpanel axis is labeled for visual purposes. Orange and purple lines denote 0 level contours of the lower and upper 95% simultaneous confidence bands (corresponding pointwise level $\alpha < 10^{-6}$), respectively.

speed. Here, we observed a shift in the running speed-theta phase interactions across the putative harmonic and slow gamma frequencies (~18–45 Hz). In the lower part of this range (~18–24 Hz), high running speed power was increased around the trough and rising phase of theta ($\pm\pi$). Beginning around 25 Hz, a transition occurred as high running speed power became increasingly associated with the preferred phase of slow gamma (i.e., ~0-π; Fig. 3*D*). A theta phase shift of slow gamma power with respect to running speed is also evident. This effect is weakly evident in the lower frequencies of fast gamma (~57–72 Hz) as well, but it is mostly absent throughout the majority of the fast gamma range (>72 Hz). The interpretation of these effects is complicated by coincident changes in the theta waveform shape, which can obscure theta phase estimates, and associated theta harmonics, which can obscure gamma power estimates. However, our findings are generally in line with those of Chen et al. (2011) and demonstrate the strength of the additive model approach taken here.

Experience-dependent changes in theta and slow gamma. To assess the influence of experience on theta and gamma rhythms, we fit a sequence of five additional models by incorporating *time-within-session* (also referred to as *time*), *session number*, and their corresponding interactions as predictors. We compared the predictive performances of these models using a leave-one-mouse-out cross-validation approach. Figures 4, 5, and 7 show the additive contributions of each of these terms in the *full* model (see MATERIALS AND METHODS) that were not included in the *base* model discussed above. These include the *time-by-session*, *running speed-by-time-by-session*, and *theta phase-by-time-by-session* interactions. Incorporating these additional predictors did not alter the estimated effects for the terms in the *base* model ($\rho_{base,\ full} > 0.99$ for *running speed, theta phase*, and *running speed-by-theta phase*). Figure 4*A* shows the additive contribution of *time* for each of the three sessions, while Fig. 4*B* displays the corresponding between-session comparisons of these contributions in the form of difference surfaces. Fast theta, slow gamma, and fast gamma power displayed significant trends over time in all three sessions (Fig. 4*A*). Power for fast theta (~10 Hz) and its putative harmonic (~20 Hz) decreased over time in all three sessions (Fig. 4*A*), and the elevated power at the beginning of the sessions for these frequencies was significantly greater in *session 1* compared with *sessions 2* and *3* (Fig. 4*B*). Conversely, slow theta power was significantly reduced in the initial portion of *session 1* but not *sessions 2* and *3* (Fig. 4*A*). A different pattern was observed for slow gamma power. Like fast theta, slow gamma power decreased over time in *sessions 2* and *3* (Fig. 4*A*). However, this effect was absent in *session 1* in which slow gamma was transiently diminished early in the session (Fig. 4*A*, left). Accordingly, there was a significant difference between slow gamma power in the initial period of the first, relative to the second and third sessions, and slow gamma power at the start of the second and third sessions were not significantly different (Fig. 4*B*). Fast gamma power significantly decreased across time in all three sessions (Fig. 4*A*), and no significant differences in fast gamma power were

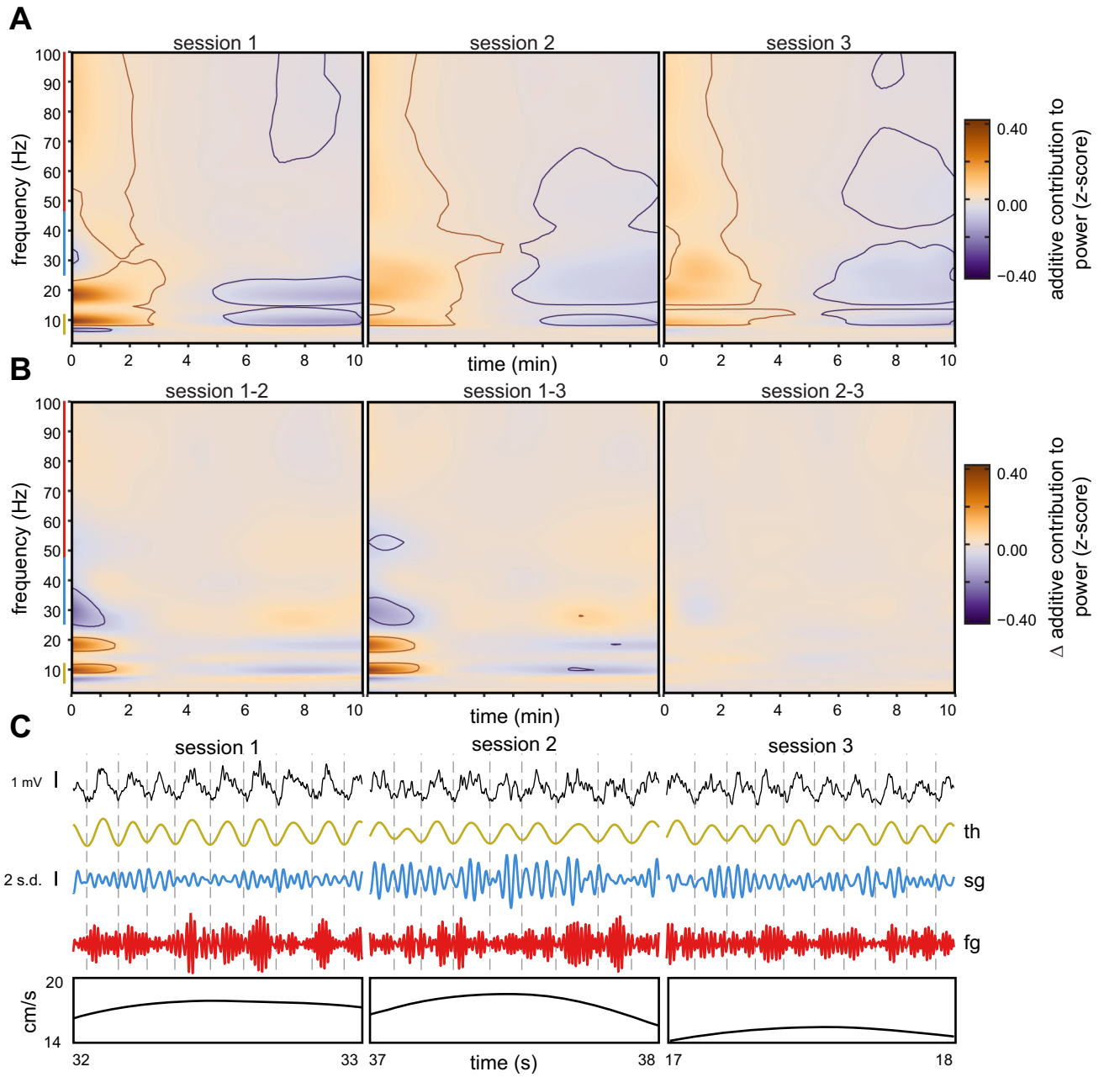

Fig. 4. Experience-dependent trends in theta and gamma power. *A*: additive contribution of *time-by-session* to power at each frequency fit under the *full* model (see text). *B*: differences between the surfaces shown in *A*. The *left* subpanel shows the *session 2* surface subtracted from the *session 1* surface, while the *middle* and *right* subpanels show the *session 3* surface subtracted from the *session 1* and *session 2* surfaces, respectively. For both *A* and *B*, the axes on the middle subpanels are not labeled for visual purposes. Orange and purple lines denote 0 level contours of the lower and upper 95% simultaneous confidence bands (corresponding pointwise level $\alpha < 10^{-6}$), respectively. Yellow, blue, and red lines on frequency axes denote approximate theta, slow gamma, and fast gamma bands, respectively. *C*: example LFP recordings (*top row*) from a representative electrode, and bandpass-filtered versions for theta (th), slow gamma (sg), and fast gamma (fg) frequencies, during one second intervals within the first minute of *sessions 1–3* for which animals ran at similar speeds (*bottom row*). The vertical dashed lines denote theta troughs. Note how theta amplitude is largest in *session 1*, whereas slow gamma amplitude is lowest in *session 1*.

seen between any of the sessions (Fig. 4*B*). Overall, no differences were observed at any time or frequency between *sessions 2* and *3* (Fig. 4*B*, right). Figure 4*C* shows an example LFP recording during a representative one-second period with similar running speed profiles, occurring early in *sessions 1–3*. Consistent with the results above, theta appears larger in *session 1*, whereas slow gamma appears larger in *sessions 2* and *3*. These results raise the possibility that increased fast theta power during the period of initial exposure to a familiar environment within each day may play a role in the acquisition of anticipatory firing that also occurs during this time period. Moreover, the recovery of slow gamma power that occurs after each day's initial exposure to a familiar environment may reflect an increase in the effective CA3 input to CA1 that develops with experience.

Experience-dependent trends in the influence of running speed on theta and gamma rhythms. Figure 5 shows the additive contributions of the *running speed-by-time* interaction

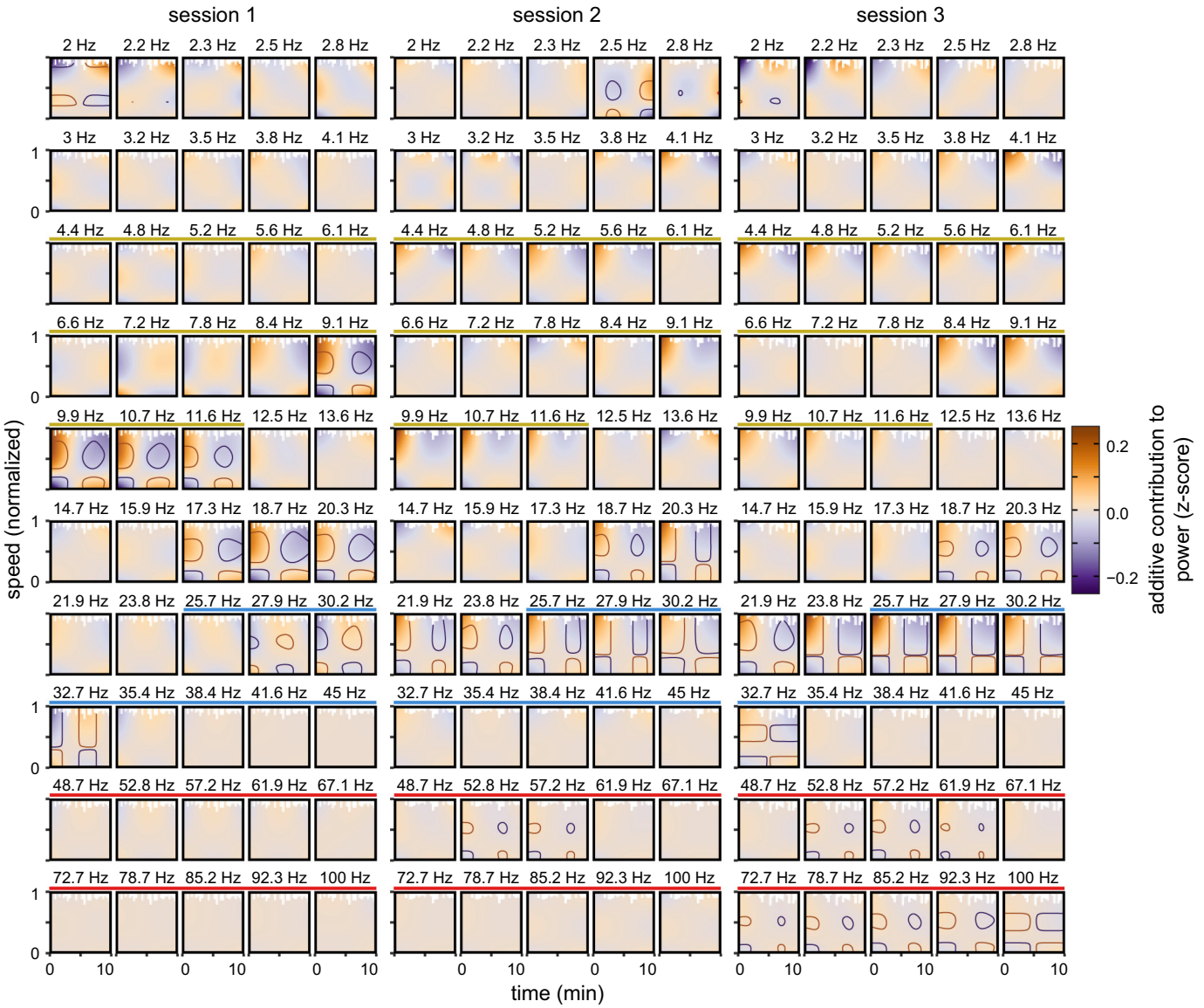

Fig. 5. Experience-dependent trends in the speed modulation of theta/gamma amplitude. Additive contribution of the *running speed-by-time* interaction to power for each frequency and session fit under the *full* model. *Left*, *middle*, and *right* panels correspond to *sessions 1–3*, respectively. Each subpanel corresponds to a separate frequency, denoted by the labels above the subpanels, logarithmically spaced between 2 and 100 Hz. Only every other subpanel axis is labeled for visual purposes. Unvisited pixels are colored white. Orange and purple lines denote 0 level contours of the lower and upper 95% simultaneous confidence bands (corresponding pointwise level $\alpha < 10^{-6}$), respectively. Yellow, blue, and red lines above individual subpanels denote frequencies within the theta, slow gamma, and fast gamma bands, respectively.

to the power of each frequency during each session. To interpret this figure, it is important to remember that each of the contributions here are additive with respect to the corresponding contributions from the main effects of running speed for each frequency (see Fig. 3*B*). Thus it communicates how the strength of the running speed modulation of power at each frequency changes slowly over time in each of the three sessions. For example, Fig. 3*B* shows that power in the fast theta (~9–10 Hz) range, and in the range of its putative harmonic (~17–20 Hz), increased with running speed, so Fig. 5 shows that this increase was significantly greater in the earlier part of *session 1* and became significantly weaker at later times in the session. As the color-coded z-score range in Fig. 3*B* is larger than that in Fig. 5 (~-0.6–0.6 in Fig. 3*B*, ~-0.25–0.25 in Fig. 5), it is not the case that total predicted power for fast theta is decreased at high running speeds in the latter half of *session 1*, but rather that the gain of the effect observed in Fig. 3*B* is mitigated. Similar tendencies were observed in *sessions 2* and *3*, but the decrease in the running speed modulation of fast theta was not identified as significant in these later sessions according to our criteria.

As was the case for the simple effects of *time-by-session* (Fig. 4), a different pattern of *running speed-by-time* interaction effects was observed for slow gamma. Figure 3*B* shows that slow gamma power increased with running speed. Unlike with theta, however, the magnitude of this power increase for slow gamma was significantly reduced early in *session 1* and became significantly greater over time within the session (Fig. 5). Conversely, in *sessions 2* and *3*, the running speed modulation of slow gamma power was greater in the early parts of

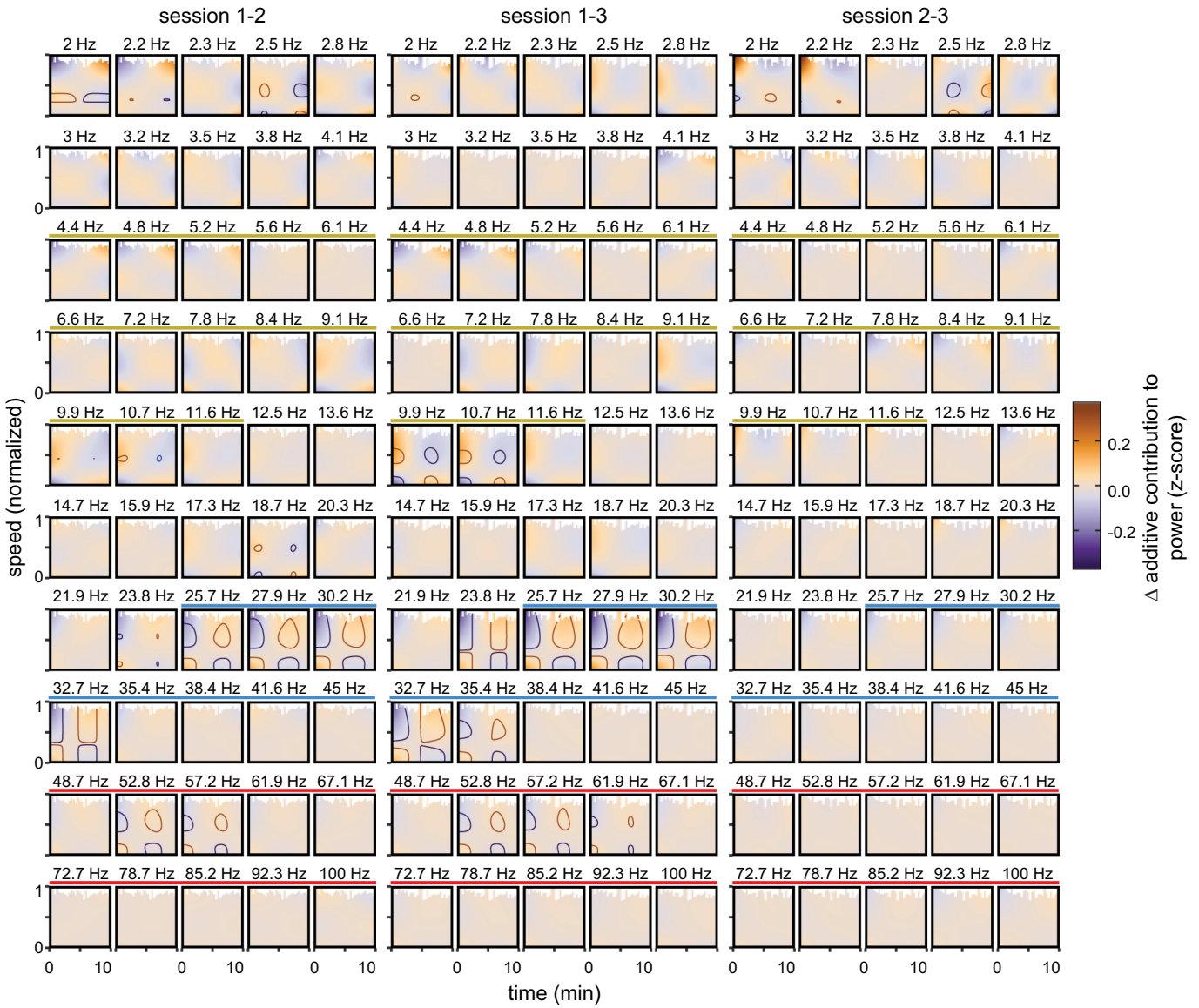

Fig. 6. Across-session differences in experience-dependent trends in the speed dependence of theta/gamma amplitude. Between-session differences for the surfaces shown in Fig. 5. *Left*: *session 2* surfaces subtracted from the *session 1* surfaces. *Middle* and *right*: *session 3* surfaces subtracted from the *session 1* and *session 2* surfaces, respectively. As in Fig. 5, each subpanel corresponds to a separate frequency, denoted by the labels on top. Pixels not visited in both sessions are colored white. Orange and purple lines denote 0 level contours of the lower and upper 95% simultaneous confidence bands (corresponding pointwise level $\alpha < 10^{-6}$), respectively. Yellow, blue, and red lines above subpanels indicate frequencies within the theta, slow gamma, and fast gamma ranges, respectively.

the sessions and became significantly reduced over time (Fig. 5). A different pattern of results was observed for fast gamma. While fast gamma power increased with running speed, as was shown in Fig. 3*B*, no significant trends in the magnitude of this increase were observed over time within *session 1* (Fig. 5). In *sessions 2* and *3*, however, small but significantly negative trends in the magnitude of running speed modulation of fast gamma power were observed (Fig. 5).

Figure 6 shows between-session comparisons of the *running speed-by-time* interactions in the form of difference surfaces for each frequency. Again, no significant differences at theta or gamma frequencies were observed between *sessions 2* and *3*, and differences between the first session and subsequent sessions were most prominent in the slow gamma range (Fig. 6). These results suggest that the running speed modulation of slow gamma power changed with experience both within and between sessions. Some small, but significant, differences were observed between all three sessions at low frequencies (<3 Hz), but these effects did not generalize to withheld data (Fig. 8) and may be explained by the stronger residual autocorrelation at these frequencies, which was not fully reduced by the AR1 process (Fig. 2).

Experience-dependent trends in theta-gamma phase-amplitude correlations. Figure 7*A* shows the additive contribution to power from the *theta phase-by-time* interactions for each frequency and session, while Fig. 7*B* displays the associated between-session difference surfaces for these effects. Both slow and fast gamma power were significantly higher at the rising phase of theta in the early parts of all three sessions (Fig. 7*A*). Again, these effects are additive with those reported earlier (i.e., in Fig. 3*C*), and the effect sizes are different (~−0.4–0.4 in Fig. 3*C* vs. ~−0.15–0.15 in Fig. 7*A*). Thus Fig.

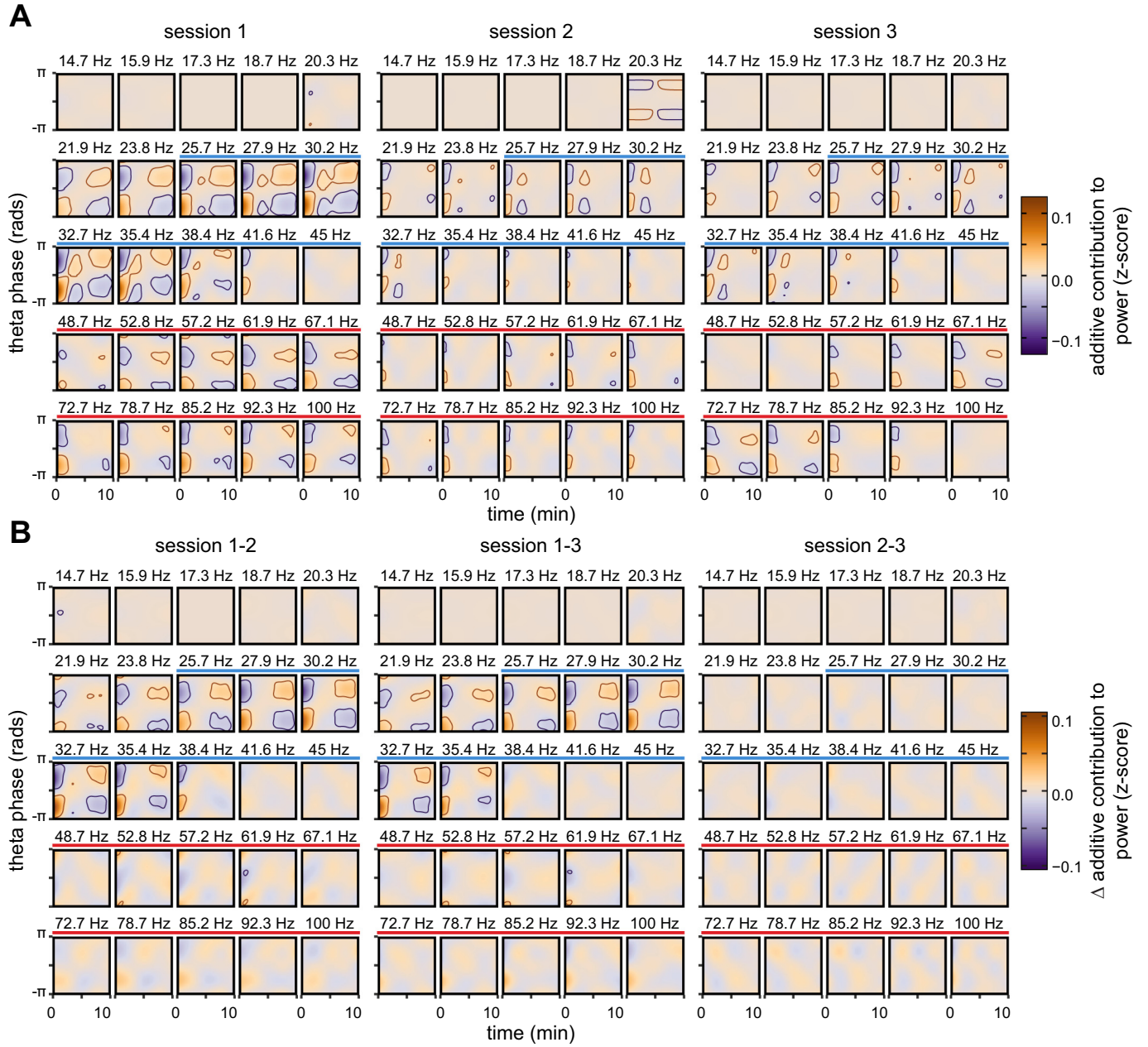

Fig. 7. Experience-dependent trends in theta phase-gamma amplitude correlations. *A*: additive contribution of the *theta phase-by-time* interaction to power for each frequency and session fit under the *full* model. *Left*, *middle*, and *right panels* correspond to *sessions 1–3*, respectively. Each subpanel shows the additive effect for a separate frequency, denoted by the labels above the subpanels. *B*: difference surfaces for the fits shown in *A*. *Left*: *session 2* surfaces subtracted from the *session 1* surfaces. *Middle* and *right*: *session 3* surfaces subtracted from the *session 1* and *session 2* surfaces, respectively. Only every other subpanel axis is labeled for visual purposes. Orange and purple lines denote 0 level contours of the lower and upper 95% simultaneous confidence bands (corresponding pointwise level $\alpha < 10^{-6}$), respectively. Blue and red lines above subpanels indicate frequencies within the slow gamma and fast gamma bands, respectively. Frequencies <14.7 Hz are omitted, as no significant effects were observed at these frequencies.

7*A* demonstrates that slow gamma power was reduced at its preferred theta phase early in the sessions, resulting in slightly weaker phase-amplitude correlations during these times. This effect was significantly larger in *session 1* compared with *sessions 2* and *3* (Fig. 7*B*). The interpretation for fast gamma is subtler and is consistent with a slight shift from the peak to the rising phase of theta early in the sessions. No between session differences were detected for fast gamma, and there were no differences between *sessions 2* and *3* at any frequency (Fig. 7*B*). As with Fig. 3*D*, the interpretation of these effects is complicated by potential influences from changes in the shape of the theta waveform and associated harmonics. However, as with the *time-by-session* and *running speed-by-time-by-session* results reported in the previous sections, experience-dependent trends in *theta phase* correlations were confined to the slow gamma range. It is possible that additional trends exist with regard to running speed modulation of theta phase correlations over time, considering the running speed results shown in Fig. 5. However, we did not explore this effect as it requires estimation of a complicated four-way interaction.

Cross-validation. We next compared the predictive performance of the different variables on out-of-sample data using a

leave-one-mouse-out cross-validation approach (see *Cross-validation analyses* section in MATERIALS AND METHODS). Six models of varying levels of complexity, ranging from the *base* to the *full* models discussed previously, were compared. For all models, cross-validated R^2 values were typically low (<0.08; Fig. 8). This can be partially attributed to the noisiness of LFPs, and to inter-animal variability; however, it also highlights a need for additional research into the statistical modeling of these signals. Despite the small R^2 values, clear peaks in predictive performance are evident at slow theta (~5–7 Hz), fast theta (~9–10 Hz), and their putative harmonics at ~12–13 Hz and ~17–20 Hz. In addition, large and separate slow gamma (~25–50 Hz) and fast gamma (~60–100 Hz) peaks in predictive performance are also apparent. Figure 8*B* shows the improvement in R^2 gained by including each additional variable. For example, "+ *time*" indicates the improvement beyond the *base* model when the *time* variable is included, "+ *time-by-session*" indicates the improvement beyond the + *time* model when the *time-by-session* variable is included, etc. None of the models had positive improvement at frequencies <3 Hz and ~8 Hz (Fig. 8*B*), suggesting that the predictors not included in the *base* model did not generalize well to withheld data at these frequencies. Adding *time* as a predictor improved performance at all remaining frequencies, while incorporating *time-by-session* (i.e., a separate *time* effect for each *session*) offered further improvements in the fast theta, putative fast theta harmonic, and slow gamma ranges (Fig. 8*B*). The *full* model also performed best in the fast theta, putative fast theta harmonic, and slow gamma ranges, but incorporating the *speed-by-time-by-session* interaction resulted in larger improvements compared with the *theta phase-by-time-by-session* interaction (Fig. 8*B*). Overall, the model comparison conclusions here are in line with the results reported above, which suggest that experience-dependent changes are most prominent at fast theta and slow gamma frequencies.

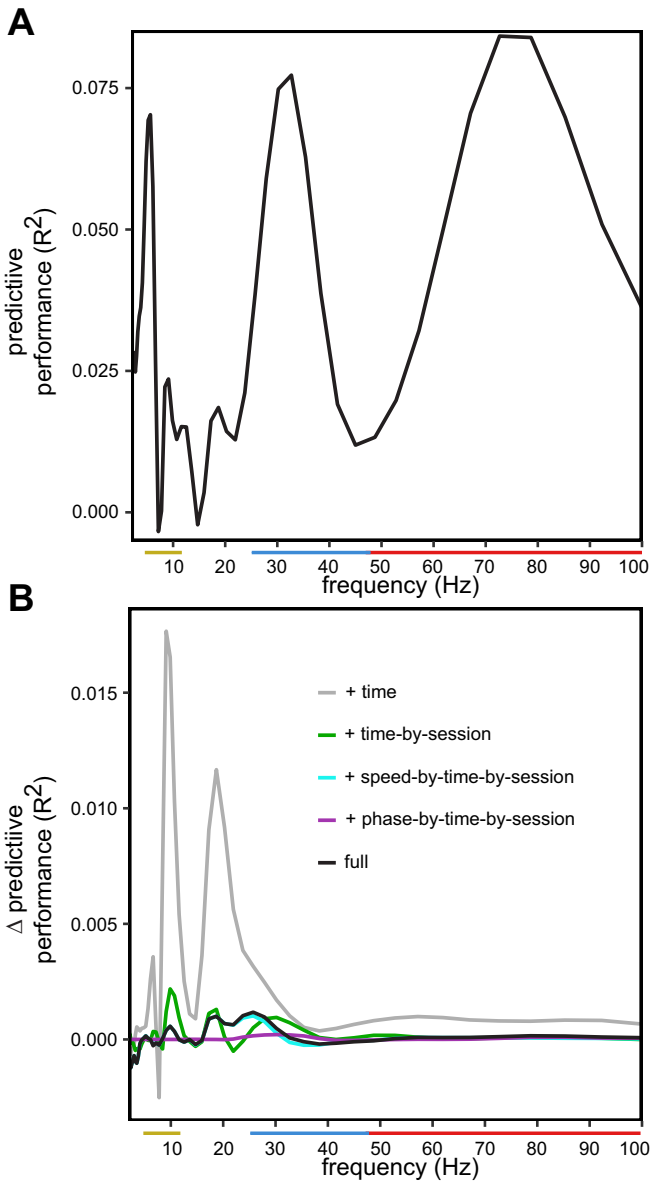

Fig. 8. Model comparisons. *A*: overall leave-one-mouse-out cross-validated R^2 for the *full* model at each frequency. *B*: improvement in R^2 due to including an additional variable. + *time* indicates improvement beyond the *base* model after adding *time*. + *time-by-session* indicates improvement beyond the + *time* model after including *time-by-session*. + *speed/phase-by-time-by-session* indicates improvement beyond the + *time-by-session* model after including *speed/phase-by-time-by-session*, respectively. Similarly, *full* indicates improvement beyond the + *time-by-session* model after including both *speed-by-time-by-session* and *phase-by-time-by-session* simultaneously. Yellow, blue, and red lines on *x*-axes denote approximate theta, slow gamma, and fast gamma frequency bands, respectively.

DISCUSSION

The acquisition of anticipatory firing in CA1 with experience in familiar environments is a robust phenomenon that has been replicated in numerous studies in both rats and mice (Cabral et al. 2014; Ekstrom et al. 2001; Lee et al. 2004; Mehta et al. 1997, 2000; Roth et al. 2012). Somewhat surprisingly, however, concomitant trends in the hippocampal LFP have not been studied in detail. Here, we report that such trends are frequency specific and can be observed as changes over time in baseline power, as well as changes over time in the dependencies between power, running speed, and theta phase. Specifically, we found that experience-dependent changes in oscillatory power were concentrated in the frequency ranges associated with previously reported hippocampal oscillations (i.e., slow theta, fast theta, slow gamma, fast gamma). Moreover, experience-dependent changes in oscillatory power were strongest at theta and slow gamma frequencies. Baseline power was transiently enhanced for running-related fast theta, and transiently diminished for slow gamma, in the first minutes of exposure to a familiar environment each day. This is the same period during which anticipatory firing is acquired in CA1 place cells. Similarly, the influence of running speed on oscillatory power was transiently enhanced for theta, and diminished for slow gamma, during this same time period. In addition, the influence of theta phase on slow gamma power was also transiently altered. In contrast, fast gamma displayed trends across time within a session that were nearly identical across repeated sessions within a day. Therefore, fast gamma appears to be less influenced by experience than slow gamma or fast theta.

It is possible that experience-dependent trends in oscillatory patterns may provide insights about the emergence of anticipatory firing in CA1 place cells. Our results showed a selective enhancement of oscillatory power in the fast theta range during the initial period of each day's first testing session (Fig. 4), a time period during which synaptic plasticity that is thought to underlie

anticipatory firing (Mehta et al. 2000) presumably emerges. It is possible that strong theta activity in CA1 during this time promotes synaptic plasticity in CA1 synapses (Larson et al. 1986; Staubli and Lynch 1987). Once expressed, such plastic changes could allow place cells to fire in response to lower levels of excitatory input, thereby allowing place cells to fire earlier in their place fields. Others have suggested higher theta frequencies may act as a mechanism to increase the sampling rate of sensory information during locomotion (Fuhrmann et al. 2015). Such a mechanism could also be utilized during periods of elevated attention or general arousal, which may be increased during early exposures to an environment.

Experience-dependent increases in slow gamma power may result from plasticity in CA3–CA1 synapses, signaling an increase in the effective influence of CA3 over CA1. On the other hand, a lack of slow gamma may prevent anticipatory firing in CA1 place cells. We observed a selective suppression of slow gamma during the first moments of the first session of each day that was not observed in later sessions (Fig. 4). Anticipatory firing is often interpreted as a kind of memory retrieval process at the single cell level, with CA1 place cells retrieving the stored memory of a spatial location from CA3 slightly before the location is actually reached (Bieri et al. 2014; De Almeida et al. 2012). Considering that slow gamma is thought to facilitate transmission of information from CA3 to CA1 in both mice (Chen et al. 2011; Lasztóczi and Klausberger 2014, 2016; Yamamoto et al. 2014) and rats (Belluscio et al. 2012; Colgin et al. 2009; Kemere et al. 2013; Schomburg et al. 2014), the reduction of slow gamma at the beginning of the first session of each day may reduce transmission of information from CA3 to CA1 and thereby prevent anticipatory firing in CA1.

This viewpoint and the present results are broadly consistent with those of Bieri et al. (2014), who reported a link between place cell anticipatory firing and slow gamma power in rats. The present results provide evidence that such a link between anticipatory firing and slow gamma rhythms is also present in mice. However, given the differences between gamma in mice and rats (Ahmed and Mehta 2012; Buzsáki et al. 2003; Chen et al. 2011), it remains to be determined whether all or any of the experience-dependent effects discussed here also pertain to rats. A recent study in rats reported weaker slow gamma and stronger fast gamma modulation of CA1 place cell spiking during early trials on a familiar linear track (Fernández-Ruiz et al. 2017), which is generally in line with the present results in mice. These effects were interpreted as support for a stronger entorhinal drive to CA1 during early exposures to an environment. Expanding upon this interpretation, our results suggest that this increased entorhinal drive becomes better matched by a stronger CA3 drive upon repeated exposures within a day.

Overall, these results motivate a number of predictions. First, if fast theta-mediated synaptic plasticity underlies the acquisition of anticipatory firing, then disruption of fast theta-generating circuits during the initial part of an experience should prevent or delay the acquisition of anticipatory coding in CA1. Similarly, if slow gamma is enhanced by fast theta-mediated plasticity, then disruption of fast theta during the initial part of an experience should prevent or delay the emergence of slow gamma. On the other hand, disruption of fast theta at later points in an experience should reduce slow gamma power to a lesser extent, or slow gamma power should recover more quickly after a transient reduction. Additionally, if the emergence of slow gamma promotes anticipatory firing, then disruption of slow gamma-generating circuits at any time during an experience should prevent anticipatory firing. Although precise control over the slow gamma rhythm remains elusive, Blumberg and colleagues (2016) have recently shown that 30 Hz stimulation of the medial septum produces 30-Hz oscillations in the hippocampus. Moreover, efforts to entrain CA1 theta in mice, via optogenetic manipulation of septo-hippocampal circuits, have been fruitful (Bender et al. 2015; Fuhrmann et al. 2015). Thus these predictions may be testable and offer promising directions for future study.

ACKNOWLEDGMENTS

The authors acknowledge the Texas Advanced Computing Center (TACC) at The University of Texas at Austin for providing HPC resources that have contributed to the research results reported within this paper (https://www.tacc.utexas.edu). We thank Katelyn N. Bobbitt for contributing to drive design and Kayli Kallina for preparing histological sections. We also thank Dr. Kamal Hamidieh (Department of Statistics and Data Sciences, The University of Texas at Austin), Brian Knab, Robert Shaffer, and Chang Sun for helpful discussions and advice regarding the additive mixed model approach.

Address for L. L. Colgin: Department of Neuroscience and Center for Learning and Memory, University of Texas at Austin, 1 University Station Stop C7000, Austin, TX 78712 (e-mail: colgin@mail.clm.utexas.edu).

GRANTS

This work was supported by the Esther A. and Joseph Klingenstein Fund, Alfred P. Sloan Foundation, ONR (N00014-1-03322), Alzheimer's Association (NIRP-14-305205), the National Science Foundation Graduate Research Program under Grant No. DGE-1110007 (to B. J. Gereke), and the National Institute on Drug Abuse (primary) of the National Institutes of Health under award number T32DA018926 (to B. J. Gereke).

DISCLOSURES

No conflicts of interest, financial or otherwise, are declared by the authors.

AUTHOR CONTRIBUTIONS

B.J.G. and L.L.C. conceived and designed research; B.J.G. and A.J.M. performed experiments; B.J.G. analyzed data; B.J.G. and L.L.C. interpreted results of experiments; B.J.G. prepared figures; B.J.G. and L.L.C. drafted manuscript; B.J.G. and L.L.C. edited and revised manuscript; B.J.G., A.J.M., and L.L.C. approved final version of manuscript.

REFERENCES

Ahmed OJ, Mehta MR. Running speed alters the frequency of hippocampal gamma oscillations. *J Neurosci* 32: 7373–7383, 2012. doi:10.1523/JNEUROSCI.5110-11.2012.

Baayen RH, van Rij J, de Cat C, Wood SN. *Autocorrelated errors in experimental data in the language sciences: some solutions offered by Generalized Additive Mixed Models* [Online]. ArXiv Prepr. ArXiv160102043, 2016. https://arxiv.org/abs/1601.02043 [3 Jan. 2017].

Belluscio MA, Mizuseki K, Schmidt R, Kempter R, Buzsáki G. Cross-frequency phase-phase coupling between θ and γ oscillations in the hippocampus. *J Neurosci* 32: 423–435, 2012. doi:10.1523/JNEUROSCI.4122-11.2012.

Bender F, Gorbati M, Cadavieco MC, Denisova N, Gao X, Holman C, Korotkova T, Ponomarenko A. Theta oscillations regulate the speed of locomotion via a hippocampus to lateral septum pathway. *Nat Commun* 6: 8521, 2015. doi:10.1038/ncomms9521.

Bieri KW, Bobbitt KN, Colgin LL. Slow and fast γ rhythms coordinate different spatial coding modes in hippocampal place cells. *Neuron* 82: 670–681, 2014. doi:10.1016/j.neuron.2014.03.013.

Blumberg BJ, Flynn SP, Barriere SJ, Mouchati PR, Scott RC, Holmes GL, Barry JM. Efficacy of nonselective optogenetic control of the medial septum over hippocampal oscillations: the influence of speed and implica-

tions for cognitive enhancement. *Physiol Rep* 4: e13048, 2016. doi:10.14814/phy2.13048.

Buzsáki G. Hippocampal sharp waves: their origin and significance. *Brain Res* 398: 242–252, 1986. doi:10.1016/0006-8993(86)91483-6.

Buzsáki G, Buhl DL, Harris KD, Csicsvari J, Czéh B, Morozov A. Hippocampal network patterns of activity in the mouse. *Neuroscience* 116: 201–211, 2003. doi:10.1016/S0306-4522(02)00669-3.

Cabral HO, Fouquet C, Rondi-Reig L, Pennartz CMA, Battaglia FP. Single-trial properties of place cells in control and CA1 NMDA receptor subunit 1-KO mice. *J Neurosci* 34: 15861–15869, 2014. doi:10.1523/JNEUROSCI.5320-13.2014.

Chen Z, Resnik E, McFarland JM, Sakmann B, Mehta MR. Speed controls the amplitude and timing of the hippocampal gamma rhythm. *PLoS One* 6: e21408, 2011. doi:10.1371/journal.pone.0021408.

Colgin LL, Denninger T, Fyhn M, Hafting T, Bonnevie T, Jensen O, Moser M-B, Moser EI. Frequency of gamma oscillations routes flow of information in the hippocampus. *Nature* 462: 353–357, 2009. doi:10.1038/nature08573.

De Almeida L, Idiart M, Villavicencio A, Lisman J. Alternating predictive and short-term memory modes of entorhinal grid cells. *Hippocampus* 22: 1647–1651, 2012. doi:10.1002/hipo.22030.

Duong T. ks: Kernel density estimation and kernel discriminant analysis for multivariate data in R. *J Stat Softw* 21: 1–16, 2007. doi:10.18637/jss.v021.i07.

Duong T. Non-parametric smoothed estimation of multivariate cumulative distribution and survival functions, and receiver operating characteristic curves. *J Korean Stat Soc* 45: 33–50, 2016. doi:10.1016/j.jkss.2015.06.002.

Dupret D, O'Neill J, Pleydell-Bouverie B, Csicsvari J. The reorganization and reactivation of hippocampal maps predict spatial memory performance. *Nat Neurosci* 13: 995–1002, 2010. doi:10.1038/nn.2599.

Ekstrom AD, Meltzer J, McNaughton BL, Barnes CA. NMDA receptor antagonism blocks experience-dependent expansion of hippocampal "place fields". *Neuron* 31: 631–638, 2001. doi:10.1016/S0896-6273(01)00401-9.

Fernández-Ruiz A, Oliva A, Nagy GA, Maurer AP, Berényi A, Buzsáki G. Entorhinal-CA3 dual-input control of spike timing in the hippocampus by theta-gamma coupling. *Neuron* 93: 1213–1226.e5, 2017. doi:10.1016/j.neuron.2017.02.017.

Foster DJ, Wilson MA. Reverse replay of behavioural sequences in hippocampal place cells during the awake state. *Nature* 440: 680–683, 2006. doi:10.1038/nature04587.

Fuhrmann F, Justus D, Sosulina L, Kaneko H, Beutel T, Friedrichs D, Schoch S, Schwarz MK, Fuhrmann M, Remy S. Locomotion, theta oscillations, and the speed-correlated firing of hippocampal neurons are controlled by a medial septal glutamatergic circuit. *Neuron* 86: 1253–1264, 2015. doi:10.1016/j.neuron.2015.05.001.

Hollup SA, Molden S, Donnett JG, Moser M-B, Moser EI. Accumulation of hippocampal place fields at the goal location in an annular watermaze task. *J Neurosci* 21: 1635–1644, 2001.

Hölscher C, Anwyl R, Rowan MJ. Stimulation on the positive phase of hippocampal theta rhythm induces long-term potentiation that can be depotentiated by stimulation on the negative phase in area CA1 in vivo. *J Neurosci* 17: 6470–6477, 1997.

Hyman JM, Wyble BP, Goyal V, Rossi CA, Hasselmo ME. Stimulation in hippocampal region CA1 in behaving rats yields long-term potentiation when delivered to the peak of theta and long-term depression when delivered to the trough. *J Neurosci* 23: 11725–11731, 2003.

Kemere C, Carr MF, Karlsson MP, Frank LM. Rapid and continuous modulation of hippocampal network state during exploration of new places. *PLoS One* 8: e73114, 2013. doi:10.1371/journal.pone.0073114.

Kramis R, Vanderwolf CH, Bland BH. Two types of hippocampal rhythmical slow activity in both the rabbit and the rat: relations to behavior and effects of atropine, diethyl ether, urethane, and pentobarbital. *Exp Neurol* 49: 58–85, 1975. doi:10.1016/0014-4886(75)90195-8.

Krivobokova T, Kauermann G. A note on penalized spline smoothing with correlated errors. *J Am Stat Assoc* 102: 1328–1337, 2007. doi:10.1198/016214507000000978.

Larson J, Wong D, Lynch G. Patterned stimulation at the theta frequency is optimal for the induction of hippocampal long-term potentiation. *Brain Res* 368: 347–350, 1986. doi:10.1016/0006-8993(86)90579-2.

Lasztóczi B, Klausberger T. Layer-specific GABAergic control of distinct gamma oscillations in the CA1 hippocampus. *Neuron* 81: 1126–1139, 2014. doi:10.1016/j.neuron.2014.01.021.

Lasztóczi B, Klausberger T. Hippocampal place cells couple to three different gamma oscillations during place field traversal. *Neuron* 91: 34–40, 2016. doi:10.1016/j.neuron.2016.05.036.

Lee I, Rao G, Knierim JJ. A double dissociation between hippocampal subfields: differential time course of CA3 and CA1 place cells for processing changed environments. *Neuron* 42: 803–815, 2004. doi:10.1016/j.neuron.2004.05.010.

Mably AJ, Gereke BJ, Jones DT, Colgin LL. Impairments in spatial representations and rhythmic coordination of place cells in the 3xTg mouse model of Alzheimer's disease. *Hippocampus* 27: 378–392, 2017. doi:10.1002/hipo.22697.

Mehta MR. From synaptic plasticity to spatial maps and sequence learning. *Hippocampus* 25: 756–762, 2015. doi:10.1002/hipo.22472.

Mehta MR, Barnes CA, McNaughton BL. Experience-dependent, asymmetric expansion of hippocampal place fields. *Proc Natl Acad Sci USA* 94: 8918–8921, 1997. doi:10.1073/pnas.94.16.8918.

Mehta MR, Quirk MC, Wilson MA. Experience-dependent asymmetric shape of hippocampal receptive fields. *Neuron* 25: 707–715, 2000. doi:10.1016/S0896-6273(00)81072-7.

O'Keefe J, Dostrovsky J. The hippocampus as a spatial map. Preliminary evidence from unit activity in the freely-moving rat. *Brain Res* 34: 171–175, 1971. doi:10.1016/0006-8993(71)90358-1.

R Core Team. *R: A language and environment for statistical computing*. Vienna, Austria: R Foundation for Statistical Computing. https://www.R-project.org/ [2016].

Roth ED, Yu X, Rao G, Knierim JJ. Functional differences in the backward shifts of CA1 and CA3 place fields in novel and familiar environments. *PLoS One* 7: e36035, 2012. doi:10.1371/journal.pone.0036035.

Ruppert D, Wand MP, Carroll RJ. *Semiparametric Regression*. Cambridge, UK: Cambridge University Press, 2003. doi:10.1017/CBO9780511755453.

Schomburg EW, Fernández-Ruiz A, Mizuseki K, Berényi A, Anastassiou CA, Koch C, Buzsáki G. Theta phase segregation of input-specific gamma patterns in entorhinal-hippocampal networks. *Neuron* 84: 470–485, 2014. doi:10.1016/j.neuron.2014.08.051.

Sheremet A, Burke SN, Maurer AP. Movement enhances the nonlinearity of hippocampal theta. *J Neurosci* 36: 4218–4230, 2016. doi:10.1523/JNEUROSCI.3564-15.2016.

Staubli U, Lynch G. Stable hippocampal long-term potentiation elicited by 'theta' pattern stimulation. *Brain Res* 435: 227–234, 1987. doi:10.1016/0006-8993(87)91605-2.

Voigts J, Siegle JH, Pritchett DL, Moore CI. The flexDrive: an ultra-light implant for optical control and highly parallel chronic recording of neuronal ensembles in freely moving mice. *Front Syst Neurosci* 7: 8, 2013. doi:10.3389/fnsys.2013.00008.

Wood SN. Stable and efficient multiple smoothing parameter estimation for generalized additive models. *J Am Stat Assoc* 99: 673–686, 2004. doi:10.1198/016214504000000980.

Wood SN. Fast stable restricted maximum likelihood and marginal likelihood estimation of semiparametric generalized linear models. *J R Stat Soc Series B Stat Methodol* 73: 3–36, 2011. doi:10.1111/j.1467-9868.2010.00749.x.

Wood SN. On P values for smooth components of an extended generalized additive model. *Biometrika* 100: 221–228, 2013. doi:10.1093/biomet/ass048.

Wood SN. *Generalized Additive Models: An Introduction with R* (2nd ed.). Boca Raton, FL: CRC Press, 2017.

Wood SN, Goude Y, Shaw S. Generalized additive models for large data sets. *J R Stat Soc Ser C Appl Stat* 64: 139–155, 2015. doi:10.1111/rssc.12068.

Yamamoto J, Suh J, Takeuchi D, Tonegawa S. Successful execution of working memory linked to synchronized high-frequency gamma oscillations. *Cell* 157: 845–857, 2014. doi:10.1016/j.cell.2014.04.009.

Yu X, Yoganarasimha D, Knierim JJ. Backward shift of head direction tuning curves of the anterior thalamus: comparison with CA1 place fields. *Neuron* 52: 717–729, 2006. doi:10.1016/j.neuron.2006.10.003.

Zaremba JD, Diamantopoulou A, Danielson NB, Grosmark AD, Kaifosh PW, Bowler JC, Liao Z, Sparks FT, Gogos JA, Losonczy A. Impaired hippocampal place cell dynamics in a mouse model of the 22q11.2 deletion. *Nat Neurosci* 20: 1612–1623; advance online publication, 2017. doi:10.1038/nn.4634.

Zheng C, Bieri KW, Trettel SG, Colgin LL. The relationship between gamma frequency and running speed differs for slow and fast gamma rhythms in freely behaving rats. *Hippocampus* 25: 924–938, 2015. doi:10.1002/hipo.22415.